IVYSPRING INTERNATIONAL PUBLISHER

Theranostics

2019; 9(7): 1893-1908. doi: 10.7150/thno.30523

Research Paper

# Tumor Chemo-Radiotherapy with Rod-Shaped and Spherical Gold Nano Probes: Shape and Active Targeting Both Matter

Lu Zhang[1], Huilan Su[2], Haolu Wang[3], Qian Li[1], Xiao Li[4], Chuanqing Zhou[1], Jia Xu[1], Yimin Chai[1], Xiaowen Liang[3]✉, Liqin Xiong[1] and Chunfu Zhang[1,5]✉

1. Shanghai Jiao Tong University Affiliated 6th Hospital, School of Biomedical Engineering, Shanghai Jiao Tong University, Shanghai 200030, China
2. State Key Laboratory of Metal Matrix Composites, School of Materials Science and Engineering, Shanghai Jiao Tong University, Shanghai 200240, China
3. The University of Queensland Diamantina Institute, The University of Queensland, Woolloongabba, QLD 4102, Australia
4. Department of Nuclear Medicine, Changhai Hospital, The Secondary Military Medical University, Shanghai 200433, China
5. Department of Nuclear Medicine, Rui Jin Hospital, School of Medicine, Shanghai Jiao Tong University, Shanghai 200025, China

✉ Corresponding authors: Chunfu Zhang, E-mail: cfzhang@sjtu.edu.cn; Tel.: +86-21-62933323 and Xiaowen Liang, E-mail: x.liang@uq.edu.au; Tel.: +61-07-34437488



Received: 2018.10.09; Accepted: 2019.01.20; Published: 2019.03.16

## Abstract

The morphologies of gold nanoparticles (NPs) affect their tumor accumulation through enhanced permeability and retention effect. However, detailed information and mechanisms of NPs' characteristics affecting tumor accumulation are limited. The aim of this study is to evaluate the effects of shape and active targeting ligands of theranostic NPs on tumor accumulation and therapeutic efficacy, and to elucidate the underlying mechanism.

**Methods:** $\alpha v\beta 3$ integrin-targeted, cisplatin-loaded and radioisotope iodine-125 labeled spherical and rod-shaped gold nano theranostic probes (RGD-$^{125}$IPt-AuNPs and RGD-$^{125}$IPt-AuNRs) with similar sizes were fabricated and characterized. The *in vivo* distribution and chemo-radio therapeutic efficacy against tumors of these newly developed probes were subsequently evaluated. Moreover, a physiologically based pharmacokinetic (PBPK) model was developed to characterize the *in vivo* kinetics of these probes at the sub-organ level, and to reveal the mechanism of NPs' shape and active targeting ligands effects on tumor accumulation.

**Result:** Cisplatin and iodine-125 were loaded sequentially onto the NPs through a thin polydopamine coating layer on the NPs. Both RGD-$^{125}$IPt-AuNPs and RGD-$^{125}$IPt-AuNRs exhibited high specificity for $\alpha v\beta 3$ *in vitro*, with the rod-shaped probe being more efficient. The PBPK model revealed that rod-shaped gold NPs diffused more rapidly in tumor interstitial than the spherical ones. Tumor accumulations of non-targeted and rod-shaped RAD-$^{125}$IPt-AuNRs was higher in short term (1 h post injection), but not pronounced and similar to that of non-targeted spherical RAD-$^{125}$IPt-AuNPs in 24 h after intravenous injection, revealing that the NPs' shape did not have a significant impact on tumor accumulations through enhanced permeability and retention (EPR) effect in long-term. While for actively targeted NPs, in addition to a higher distribution coefficient, RGD-$^{125}$IPt-AuNRs also had a much higher tumor maximum uptake rate constant than RGD-$^{125}$IPt-AuNPs, indicating both the shape and active targeting ligands affected the tumor uptake of rod-shaped NPs. As a result, RGD-$^{125}$IPt-AuNRs had a more effective inhibition of tumor growth than RGD-$^{125}$IPt-AuNPs by chemo-radiationtherapy.

**Conclusion:** Our study suggests that both the shape and active targeting ligands of gold NPs play important roles on tumor accumulation and chemo-radio therapeutic effect.

Key words: gold nanoparticles, chemoradiotherapy, PBPK, SPECT/CT, angiogenesis targeting

## Introduction

Chemo-radiation combination therapy is a clinically well-established cancer treatment [1-3]. However, due to the poor tumor targeting and side effects of chemo drugs and the limited tolerance of radiation dose by normal tissues, chemo-radiotherapy has not been widely applied in humans in some cases [4]. To simultaneously enhance tumor accumulation of chemo drugs and radiation dose, the metal-based nanoparticles (NPs) have been explored as both the chemo drug carriers and radiosensitizers in cancer chemo-radiotherapy [5-8]. Gold NPs have been considered as an ideal platform for chemo drugs loading and radiosensitizer to improve tumor chemotherapy and radiotherapy simultaneously due to their advantages such as diversity structures, easy modification, good biocompatibility [9-11], high Z number, generation of photoelectrons and Auger electrons under irradiation [12-15].

The key factor dictating the therapeutic efficacy is tumor accumulation efficiency of the NPs. In this context, many efforts have been made to optimize tumor uptake of gold NPs using various NP sizes or shapes in variety of tumor types through enhanced permeability and retention (EPR) effect [16-18]. For instances, gold NPs with different sizes (10, 20, 30 and 50 nm) have been evaluated for tumor radiosensitization therapy, where 10 nm particles had the highest tumor accumulation and the best radiosensitization therapeutic efficacy [19]. Wang *et al* have compared different shapes of gold NPs (rod, cube and star) for tumor thermotherapy and gold nanorods showed more efficient for tumor accumulation than other shapes of NPs through EPR effect [20]. However, tumor accumulation of NPs through EPR is usually limited by physical or chemical barriers of biological systems [21-23], which performed controversially due to the heterogeneity of EPR effect across tumor locations and models [17]. NPs usually have a high accumulation in tumors of high vasculature density and permeability, but not in tumors of low vasculature density and permeability [17].

Therefore, targeting tumor angiogenesis may have advantages for chemo-radiotherapy. By targeting tumor neovasculatures, the drug-loaded NPs can reach tumor without crossing blood vascular barriers. However, previous studies comparing different shapes of gold NPs for tumor accumulation and therapeutic effect *in vivo* mainly focused either on non-targeting accumulation through EPR effect or active targeting by addressing tumor cells [24, 25]. Few studies considered tumor accumulation by simultaneously targeting tumor angiogenic vessels and cells along with EPR effect. We have prepared RGD peptide-conjugated and $\alpha v\beta 3$ integrin-targeted gold NPs in three different sizes (29, 50 and 80 nm) for tumor radiotherapy by simultaneously targeting tumor cells and neovaculatures. Our results indicated that larger particles (80 nm) were more effective for cell therapy *in vitro*, while the smaller ones (29 nm) were more effective for tumor inhabitation *in vivo* due to much higher tumor accumulation [26]. However, it is still unclear that how the shape effects on gold NP accumulation efficiency in tumors, intra-tumor kinetics, and chemo-radiotherapy efficacy when simultaneously targeting tumor cells and neovasculatures along with EPR effect.

In this study, we developed $\alpha v\beta 3$-targeted, cisplatin-loaded, radioisotope iodine-125 labeled spherical (RGD-$^{125}$IPt-AuNPs) and rod-shaped (RGD-$^{125}$IPt-AuNRs) gold nano theranostic probes, and investigated their tumor accumulation and the efficacy of chemo-radiotherapy. A physiologically based pharmacokinetic (PBPK) model was also developed to elucidate the intra-tumor kinetics of developed probes and the mechanism of shape and active targeting ligands of NPs effecting on their tumor accumulation at the sub-organ level.

## Results

### Synthesis and Characterization of RGD-$^{125}$IPt-AuNPs and RGD-$^{125}$IPt-AuNRs

Gold nanospheres (AuNPs) and nanorods (AuNRs) with uniform sizes were prepared according to previous reports [26, 27]. AuNPs were 56.37 ± 3.04 nm in diameter (Figure S1A) and AuNRs were 22.41 ± 1.01 nm in diameter and 56.12 ± 3.22 nm in length (aspect ratio of ~2.5, Figure S1B). During the synthesis, a dense polyvinyl pyrrolidone (PVP) coating on AuNPs and cetyltrimethyl ammonium bromide (CTAB) on AuNRs were formed. As a result, zeta potentials of AuNPs and AuNRs were -8.49 ± 2.58 mV and 31.01 ± 4.07 mV, respectively (Table S1). For preparation of the theranostic probes, both AuNPs and AuNRs were firstly coated with a thin layer of poly dopamine (PDA) (Figures 1A and B, Figures S1C and D) [28]. The zeta potentials of PDA-coated AuNPs (PDA-AuNPs) and AuNRs (PDA-AuNRs) were 24.93 ±5.23 mV and 22.31±2.68mV, respectively. Subsequently, PDA-AuNPs and PDA-AuNRs were further modified by amino-poly (ethylene glycol)-thiol (MW 5000, Creative PEGworks, Chapel Hill, NC) for peptide conjugation and improving the *in vivo* behavior of the NPs [29]. After the modification, zeta potentials of the PEGylated PDA-AuNPs and PDA-AuNRs were -10.23±3.33 mV and -13.67±2.46 mV, respectively. There were 128.09±14.01 and 103.51±20.95 PEG molecules anchored on an individual AuNP and AuNR, respectively, determined by Ellman method [30, 31].

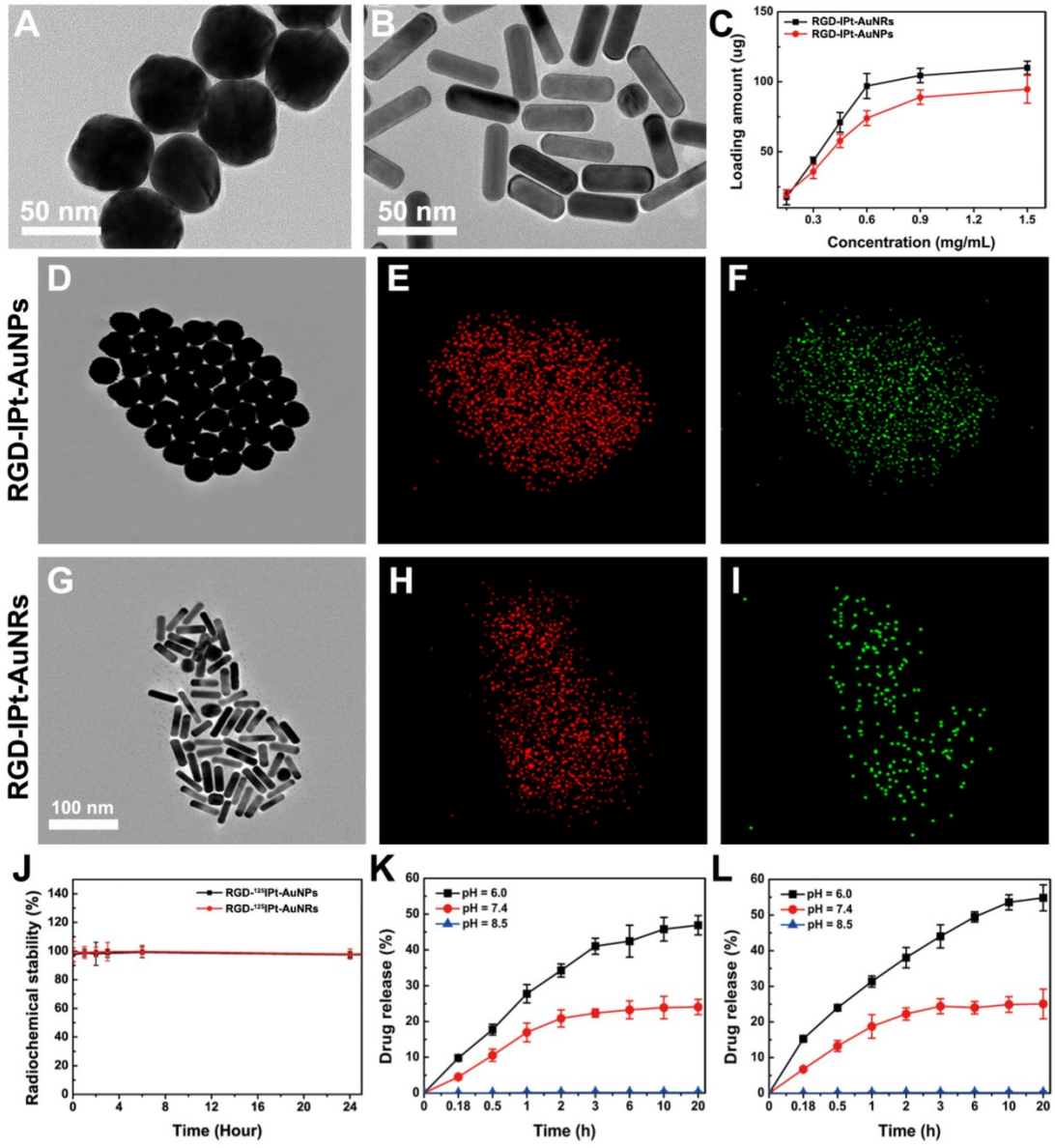


**Figure 1.** Characterization of NPs and probes. A, B: TEM images of poly dopamine coated AuNPs (A) and AuNRs (B). C: Cisplatin loading on the probes at different Pt concentrations. D-I: TEM images and EDS mapping images of gold (E, H) and platinum elements (F, I) of RGD-IPt-AuNPs (D-F) and RGD-IPt-AuNRs (G-I). J: Labeling stability of the radioisotope on surface of the probes in fetal bovine serum. K, L: The release profiles of cisplatin from RGD-IPt- AuNPs (K) and RGD-IPt-AuNRs (L) in PBS at different pH values.

By using the sulfosuccinimidyl-4-[N-maleimidomethyl]-cyclohexane-1-carboxylate (sulfo-SMCC), the PEGylated PDA-AuNPs and PDA-AuNRs were further activated and subsequently conjugated with c(RGDyC) peptides (RGD) through thiol-maleimide linkages [32], designated as RGD-AuNPs and RGD-AuNRs. The amounts of c(RGDyC) immobilized on each AuNP and AuNR were determined to be 67.33 ± 9.04 and 61.62 ± 2.15, respectively. In addition, scramble peptide c(RADyC) coupled PDA-AuNPs (RAD-AuNPs) and PDA-AuNRs (RAD-AuNRs) were also prepared as the non-targeting NPs and compared with RGD NPs to evaluate the active target efficiency using the same procedures.

After the peptide conjugation, cisplatin was loaded by suspending RGD-AuNPs or RGD-AuNRs (1 mg) into cisplatin aqueous solutions (0.3 mL) with various concentrations and stirring for at least twelve hours at the ambient temperature. The cisplatin loading efficiency was increased with the increasing in cisplatin concentration and the drug loading capacity of AuNRs was higher than that of AuNPs at each concentration (Figure 1 C). When the concentration reached 0.9 mg/mL, the drug loading capacity of AuNPs and AuNRs was 86 ± 2 μg and 108 ± 2 μg Pt per milligram of gold NPs, respectively. With further increase in cisplatin concentration, the increase in drug loading was marginal. Therefore, we loaded

both NPs at the cisplatin concentration of 0.9 mg/mL for the following studies. To confirm the presence of cisplatin on the NPs, an energy-dispersive X-ray spectroscopy element mapping (EDS) was performed (Figures 1D – 1I). Both Au (red dots) and Pt elements (green dots) located in the same region and could overlap with each other, indicating successful cisplatin loading on both AuNPs and AuNRs.

Next, the drug-loaded RGD-AuNPs (RGD-Pt-AuNPs) and RGD-AuNRs (RGD-Pt-AuNRs) were labeled with iodine-125 by mixing them (1mg in 0.3 mL) with $Na^{125}I$ (300 μCi) and vortexing for 30 min [27]. The labeling were carrier-free and confirmed by thin layer chromatography (TLC). The labeling efficiency of both types of NPs were determined to be nearly 100%. After iodine-125 labeling, the final NPs designated as RGD-$^{125}$IPt-AuNPs and RGD-$^{125}$IPt-AuNRs probes, were purified by a Sephadex G-25 chromatography with the eluent of saline. The labeling stability of radioactive $^{125}I$ on the probes was examined by suspending the probes in fetal bovine serum (FBS) at 37 °C for different time intervals. As shown in Figure 1J, detachment of iodine-125 was unnoticeable after incubation for 24 h. In addition, RGD-Pt-AuNPs and RGD-Pt-AuNRs were also labeled with non-radioactive iodine using as cold probes. Meanwhile, non-targeting NPs (RAD-Pt-AuNPs and RAD-Pt-AuNRs) were also labeled with radioactive iodine-125 (RAD-$^{125}$IPt-AuNPs, RAD-$^{125}$IPt-AuNRs) or non-radioactive iodine (RAD-IPt-AuNPs, RAD-IPt-AuNRs), which were used as control probes. The detailed probe preparation procedures were illustrated in Scheme 1.

Zeta potentials of RGD-IPt-AuNPs and RGD-IPt-AuNRs were -26.92 ± 6.17 mV and -28.44 ± 4.36 mV, respectively (Table S1). Under the physiological condition (RPMI-1640 culture medium within 10% FBS), pristine AuNPs and AuNRs began to aggregate and settle in a few minutes, and the LSPR peaks exhibited red shift (Figures S1I and J). Compared to the pristine NPs, both types of active targeting and non-targeting probes were highly stable and exhibited no significant shift of LSPR peak after incubation for 72 h (Figures S1 E - H).

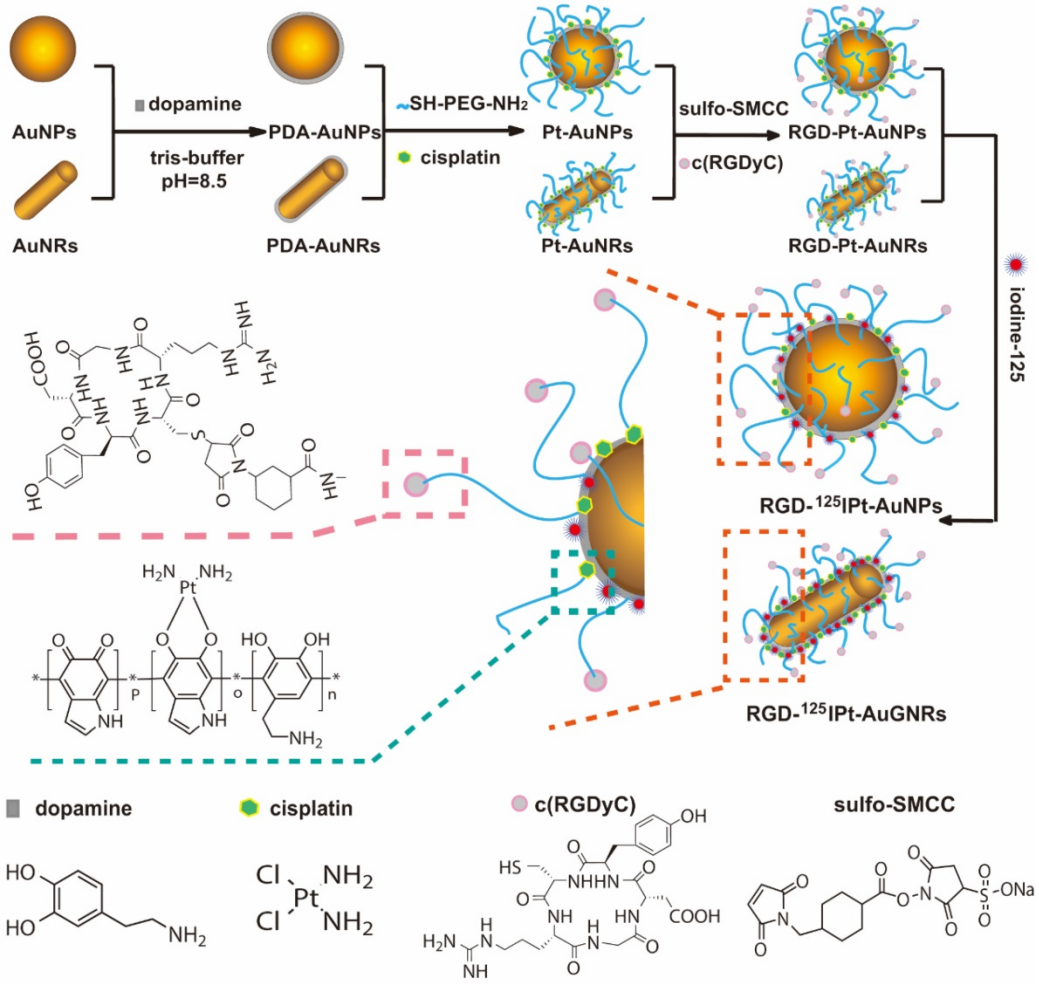


**Scheme 1.** Schematic process for synthesis of RGD probe.

To examine the cisplatin release profiles, RGD-IPt-AuNPs and RGD-IPt-AuNRs were dispersed into PBS with different pH values and incubated for different time intervals at 37 °C. As shown in Figure 1K and 1L, cisplatin release was pH-responsive. At the alkaline condition (pH 8.5), it was nearly unreleased, while at the neutral (pH 7.4) or acidic condition (pH 6), cisplatin released gradually. Consequently, 23.3 ± 1.7 % and 45.7 ± 2.3% of the loaded drug from RGD-IPt- AuNPs, and 24.5 ± 3.6 % and 54.2 ± 2.9 % from RGD-IPt-AuNRs were released after incubation for 24 hours in PBS of pH 7.4 and pH 6, respectively.

## Specificity for $\alpha v\beta 3$ Integrin

To evaluate the specificity of probes, the human derived $\alpha v\beta 3$ positive H1299 cells [33] were incubated with RGD probes (50 μg/mL, 1h), using RAD probes as the control. In addition, competition studies were also performed by incubating the cells with RGD probes in combination with free RGD peptide (10 μM). Free RGD peptide could block $\alpha v\beta 3$ integrin receptor and reduce RGD probes binding to cells if the probes had specificity for the receptor [34]. After incubation, cell uptake profiles of the probes were examined by two-photon confocal microscope and the intracellular gold contents were measured by atomic adsorption spectrophotometer (AAS). Both the microscopic images and AAS measurements indicated that cell ingested more RGD probes than RAD probes, and free RGD peptide partially suppressed the ingestion (Figure 2A and 2D). However, for the RGD probes, cell uptake of the rod-shaped probes was significantly more than that of the spherical one (RGD-IPt-AuNRs *vs* RGD-IPt-AuNPs: 56.46 ± 6.44 pg/cell *vs* 48.86 ± 4.32 pg/cell, $p < 0.05$). These results suggested that RGD probes were able to specifically target $\alpha v\beta 3$ integrin, the cell ingestion of the probes was induced partially by $\alpha v\beta 3$ integrin [35] and could be influenced by the NP shape [36]. In addition, the z-stack reconstructions of cell images from orthogonal projections using two-photon confocal microscope revealed that both probes were internalized by the cells and located quite close to the nuclei (Figure 2B and 2C).

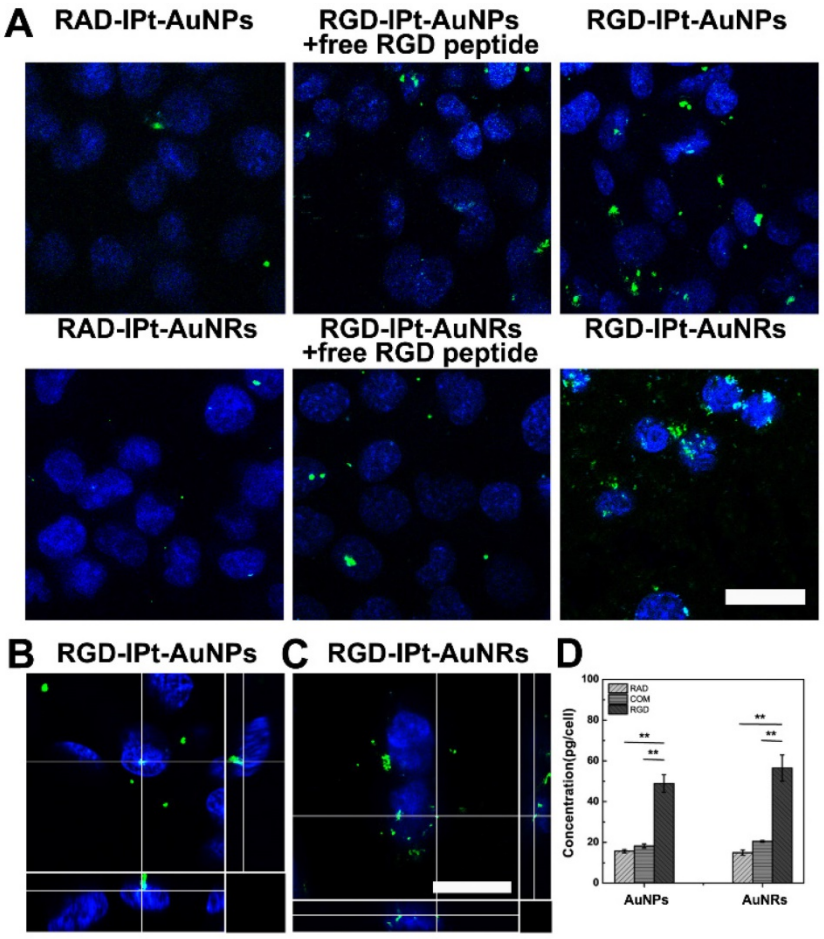


**Figure 2.** RGD-probe specificity for $\alpha v\beta 3$ positive cells. A: Two-photon microscopy images of H1299 cells after incubated with 50 μg Au /mL of probes for 1 h. B, C: The z-stack reconstructions for orthogonal projections showing the relative position of RGD-IPt- AuNPs (B) and RGD-IPt-AuNRs (C) (green) to cell body (blue, cell nuclei stained by DAPI). D: Intracellular gold contents measured by AAS. RAD: RAD probes; RGD: RGD probes; COM: RGD probes plus free peptide. **, $p < 0.01$. Scale bar: 20 μm.

## Chemotherapy and Chemoradiotherapy of Tumor Cells

The chemotherapeutic effect of the probes on tumor cells was assessed by treating H1299 cells with the RGD probes at various concentrations for 6, 24 and 48 hours. Cell viability was examined by cell counting kit-8 assay (CCK-8). No obvious cell death was observed after treatment by both types of probes at lower concentrations (< 100 μg/mL). However, dsDNA of the treated cells (50 μg/mL for 48 h) was damaged remarkably (Figure S2 D), indicating the chemotherapeutic potency of the probes. Cell death was significant when they were incubated with the probes at the concentration of 100 μg/mL for more than 24 hours (Figure S2 A-C).

In order to evaluate the chemo-radio therapeutic effect of the probes, the cells were first treated with both types of RGD probes at 50 μg/mL (in Au) for six hours, and then irradiated by 320 kV X-ray at a dose of 4 Gy (Precision X-Ray, North Branford, CT). Afterwards, the treated cells were further cultivated for different time intervals and cell viability was assayed by CCK-8. Cell viability was inhibited after radiotherapy (Figure 3). However, compared to radiation only group, pre-treated with either drug-free or drug-loaded probes resulted in a significant cell death one day after irradiation, indicating the probes have the radiosensitization effects. Four days after the treatment, cell death was more pronounced for drug-loaded probes group, even though the chemo therapeutic effect has not been observed at the same dose. However, the rod-shaped probe RGD-IPt-AuNRs were more effective than the spherical ones for both radiosensitization therapy (27.43 ± 5.72% *vs* 31.88 ± 4.79%, $p < 0.05$) and the combination therapy (10.37 ± 3.32% *vs* 14.32 ± 6.6%, $p < 0.05$) four days after the treatments.

To calculate the combination index (CI) of chemo-radiotherapy using both types of probes, the cells were incubated with both types of probes at different concentrations (10, 25, 50, 100 μg Au /mL) for 6 hours and then irradiated by X-ray for a dosage of 4 Gy. Cell viability was then examined (Figure S3). The CI values using RGD-IPt-AuNPs and RGD-IPt-AuNRs were 0.70 and 0.85, respectively, demonstrating the synergetic therapeutic effect of both types of probes.

## Specificity of RGD Probes for Tumor

To evaluate tumor specificity of the probes, SPECT/CT imaging was performed. Radioactive RGD or RAD probes were intravenously administered into H1299 tumor-bearing mice (300 μCi). The competition studies were conducted by administering the RGD probes in combination with free RGD peptide. As indicated in Figure 4A and 4B, SPECT/CT imaging demonstrated that tumor uptake of both RGD-$^{125}$IPt-AuNPs and RGD-$^{125}$IPt-AuNRs increased with the circulation time of the probes, which was noticeable one hour after probe injection and reached the maximum at 6 h after injection. However, the uptakes were significantly inhibited when competing with free RGD peptide. The tumor uptake was marginal after administrating non-targeting RAD-$^{125}$IPt-AuNPs and RAD-$^{125}$IPt-AuNRs probes in mice.

*In vivo* bio-distributions of the probes were also evaluated and quantified based on the percentage of injected dose per gram of tissue (%ID/g) (Figure 4C-D and Figure S4). In consistent with SPECT/CT imaging, both spherical and rod-shaped probes had high radiation dose in the liver and spleen, indicating they were mainly eliminated from the body through the reticuloendothelial system (RES) (Figure 4C and 4D) [37, 38]. However, the RGD probes were accumulated more in tumors than RAD ones (AuNPs probe: 5.33 ± 1.71% *vs* 2.5 ± 0.3%, $p < 0.01$; AuNRs probe: 6.93 ± 0.51% *vs* 2.67 ± 0.11%, $p < 0.01$), and the tumor accumulation was markedly decreased after competing with free RGD peptide. These results suggested that the RGD probes specifically targeted tumor $\alpha v\beta 3$ integrin receptor [39, 40]. However, the rod-shaped probes exhibited a much higher targeting efficiency than the spherical one (6.93 ± 0.51 *vs* 5.33 ± 1.71% ID/g, $p < 0.05$). The blood elimination half-lives were determined to be 227.36 ± 28.91 min and 79.99 ± 4.39 min (Figure S5 and Table S3) for RGD-$^{125}$IPt-AuNRs and RGD-$^{125}$IPt- AuNPs, respectively, using two compartment model [18]. The half-lives of RAD probes were

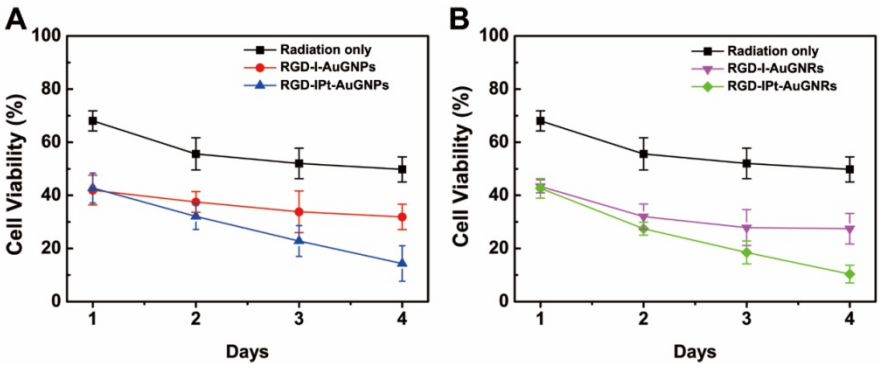


**Figure 3.** Cell viability of H1299 tumor cells after chemoradiotherapy. The cells were incubated with RGD-IPt- AuNPs (A) or RGD-IPt- AuNRs (B) at the concentration of 50 μg Au /mL for 6 h. Radiotherapy was performed by irradiating the treated cells to 4 Gy of 320 kV X-ray.

213.39 ± 22.23 min (RAD-$^{125}$IPt-AuNRs) and 94.73 ± 3.39 min (RAD-$^{125}$IPt-AuNPs), while PEG modified plain NPs were 258.22 ± 11.03 min ($^{125}$IPt-AuNRs) and 124.60 ± 12.71 min ($^{125}$IPt-AuNPs), respectively.

## Tumor Angiogenesis Targeting

Tumor angiogenesis targeting of the RGD probes was revealed by high-resolution photoacoustic imaging (PAI, Figure 5A) [41]. After intravenous injection (40 mg Au/kg), both RGD-IPt-AuNPs and RGD-IPt-AuNRs could highlight and delineate the tumor neovasculatures, indicating that RGD probes indeed registered tumor angiogenic vessels. However, the signal intensity of RGD-IPt-AuNRs increased at 1 hour post-injection, whereas the enhancement was observed 4 h after injection of RGD-IPt-AuNPs. These results suggested that RGD-IPt-AuNRs might be more efficient in tumor angiogenesis targeting than RGD-IPt- AuNPs.

To verify these observations, silver staining of tumor tissues was performed. Both tumor angiogenic vessels and cells were $\alpha v\beta_3$ positive (Figure S6). Both the spherical and the rod-shaped RGD probes could target tumor neoveculatures and cells (Figure 5B). However, RGD-IPt-AuNRs penetrated much deeper into tumor interstitial than RGD-IPt-AuNPs.

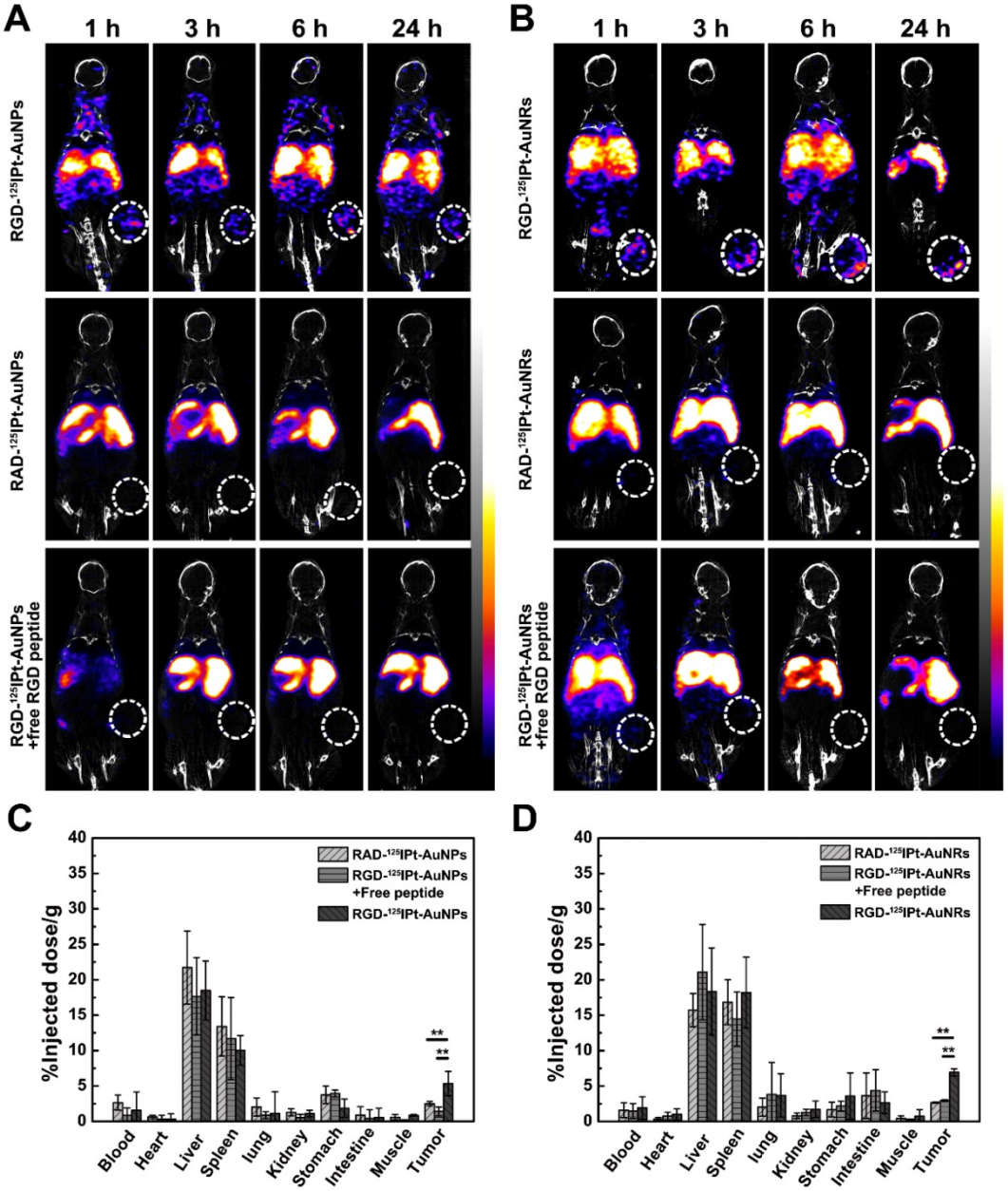


**Figure 4.** SPECT/CT imaging and bio-distributions at the organ level. A, B: SPECT/CT imaging of H1299 tumor bearing mice after intravenous administration of RGD-$^{125}$IPt- AuNPs (A) or RGD-$^{125}$IPt- AuNRs (B) (300 μCi). C, D: Bio-distributions of RGD-$^{125}$IPt- AuNPs (C) and RGD-$^{125}$IPt- AuNRs (D) 6 h after injection. **, $p < 0.01$.

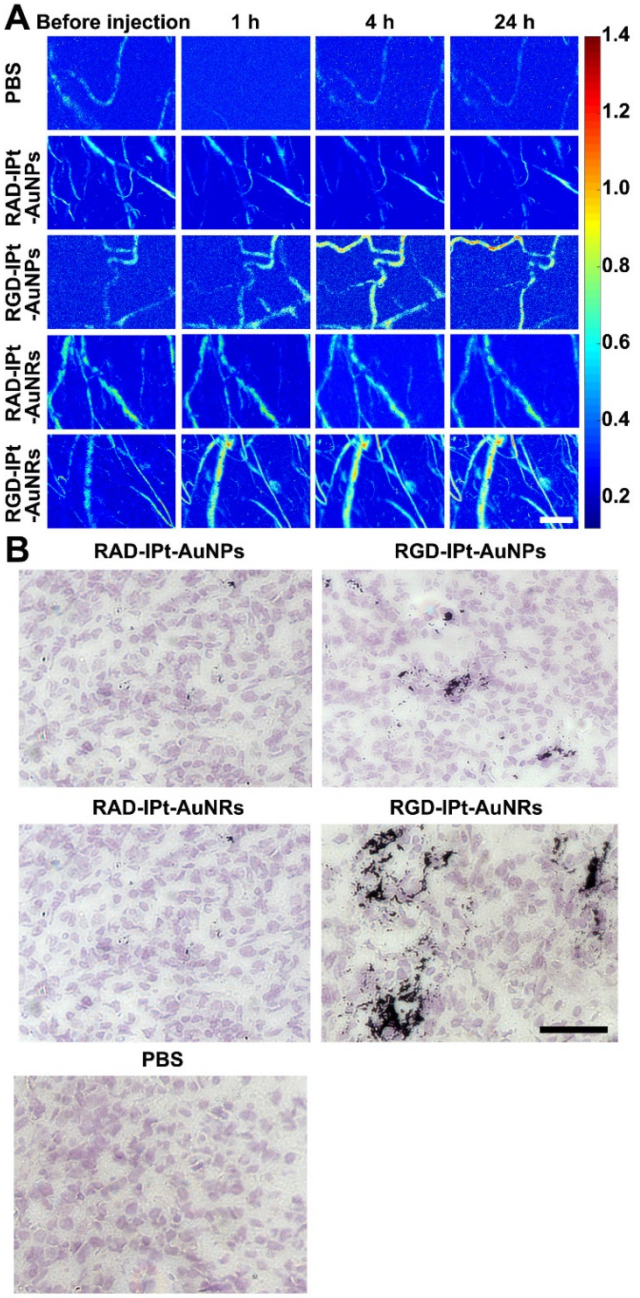


**Figure 5.** Distributions of the NPs in tumors at the sub-organ and cellular levels. A: Photoacoustic imaging of tumor regions before and after the mice were intravenously administered with both types of RGD probes using RAD probes as controls. Scale bar = 10 μm. B: Silver and hematoxylin co-staining images of the tumor tissues after PAI. Scale bar = 100 μm.

## *In vivo* Chemo-radiotherapy and Histological Studies

Since RGD probes had the high tumor accumulation efficiency, the potential of the RGD probes for tumor chemo-radiotherapy was evaluated. Tumor-bearing mice were divided into six groups (PBS, drug-free probe, drug-loaded probe, PBS + X-ray, drug-free probe + X-ray and drug-loaded probe + X-ray) and intravenously administered with RGD-IPt-AuNPs or RGD-IPt-AuNRs (40 mg Au /kg in body weight). Tumor radiotherapy was conducted six hours after probe injection for a dose of 6 Gy (320 kV, Precision X-Ray, North Branford, CT). After the treatment, the tumor volumes were monitored (Figure 6). Compared to the PBS group, chemotherapy, radiotherapy and chemo-radiotherapy with both types of probes were able to inhibit tumor growth significantly 21 days after treatment. As expected, chemo-radiotherapy was more effective than chemo or radiation therapy alone possibly due to the synergetic therapeutic effect, which is consistent with previous reports [42, 43]. However, for each therapeutic modality, RGD-IPt-AuNRs outperformed RGD-IPt-AuNPs in the therapeutic efficacy ($v/v_0$, chemotherapy: 25.47 ± 1.6 *vs* 28.63 ± 2.3, $p < 0.05$; radiation therapy: 19.74 ± 2.7 *vs* 24.8 ± 3.4 $p < 0.05$; chemoradiotherapy: 4.73 ± 0.5 *vs* 9.8 ± 2.2, $p < 0.05$).

To verify these observations, three mice from each treatment groups were sacrificed two days post the treatment and tumors were surgically removed. Immunostaining of tumor tissues against γ-H2AX was conducted and the γ-H2AX positive areas were quantified (Figure 7 and S7) [44]. It was found that both chemotherapy with drug-loaded probes and radiotherapy with drug-free probes could damage dsDNA obviously. Compared to radiotherapy without probes (PBS + radiation, γ-H2AX positive areas: 0.07 ± 0.02), radiotherapy with RGD-I-AuNPs (0.12 ± 0.04, $p < 0.01$) or RGD-I-AuNRs (0.14 ± 0.02, $p < 0.01$) significantly induced dsDNA damage, indicating that radiation dose was increased by gold NPs. Chemo-radiotherapy with RGD-IPt-AuNPs or RGD-IPt-AuNRs demonstrated synergetic therapeutic effect, inducing dsDNA damage more pronounced than chemotherapy (AuNPs probe: 0.21 ± 0.02 *vs* 0.13 ± 0.02; AuNRs probe: 0.26 ± 0.05 vs 0.15 ± 0.03, $p < 0.05$) or radiotherapy (AuNPs: 0.21 ± 0.02 *vs* 0.12± 0.04; AuNRs: 0.26 ± 0.05 vs 0.14 ± 0.02, $p < 0.05$) alone, and RGD-IPt-AuNRs was more potent than RGD-IPt-AuNPs (0.26 ± 0.05 *vs* 0.21 ± 0.02, $p < 0.05$).

Twenty-one days after the treatment, all the treated mice were euthanized. Major organs were stained by hematoxylin and eosin staining (H&E) for histological examinations (Figure S8). The H&E images did not reveal noticeable damage in organs, indicating these treatments did not have obvious toxic effects to normal tissues *in vivo*.

## Suborgan Kinetics of AuNPs and AuNRs in the Tumor

To elucidate the underlying mechanism that RGD-IPt-AuNRs had a better performance for tumor chemo-radiotherapy than RGD-IPt-AuNPs, we developed a PBPK model to characterize the intra-tumor

kinetics of the two types of probes. The model structure was based on all of the above experimental data and the published intravital details of the injected NPs [45, 46]. It consists of eight compartments: venous blood, arterial blood, liver, lung, tumor, kidneys, spleen, and rest of body (Figure 8A). As shown in previously published PBPK models [45, 46], the bio-distribution of NPs was assumed to be governed by two processes: (a) the ability to cross the capillary membrane of the organs and (b) to be taken up by endocytosis. The transportation of NPs from the blood to the tissue compartments was described with membrane-limited (also termed diffusion-limited) models. The uptake rate constant was time-dependent and described by a Hill equation to adequately describe a fraction of NPs sequestered by tumor cells with time.

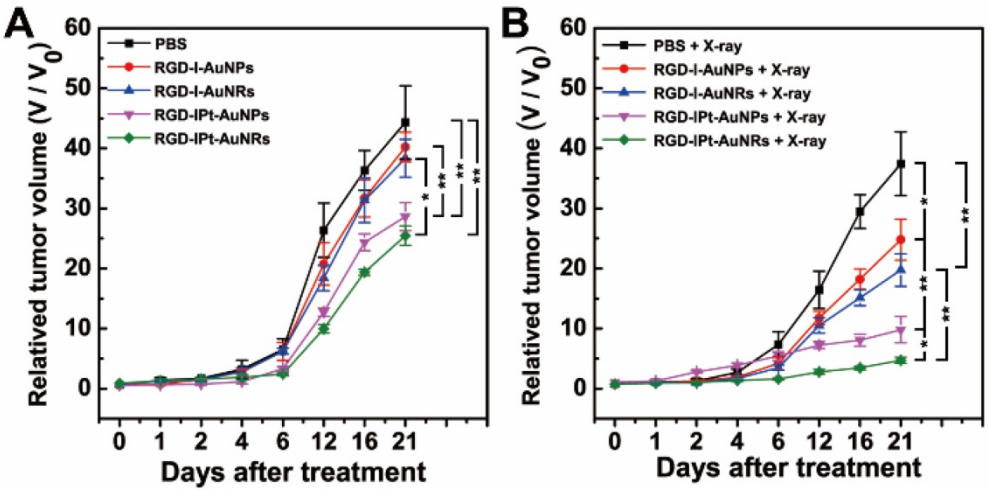


**Figure 6.** Tumor size after chemoradiotherapy. A, B: Growth curves of tumors after tumor-bearing mice were treated with both AuNPs and AuNRs probes (40 mg Au /kg b. w) (A) or with the probes plus X-ray radiations (320 kV, 6Gy) (B). *, $p < 0.05$; **, $p < 0.01$.

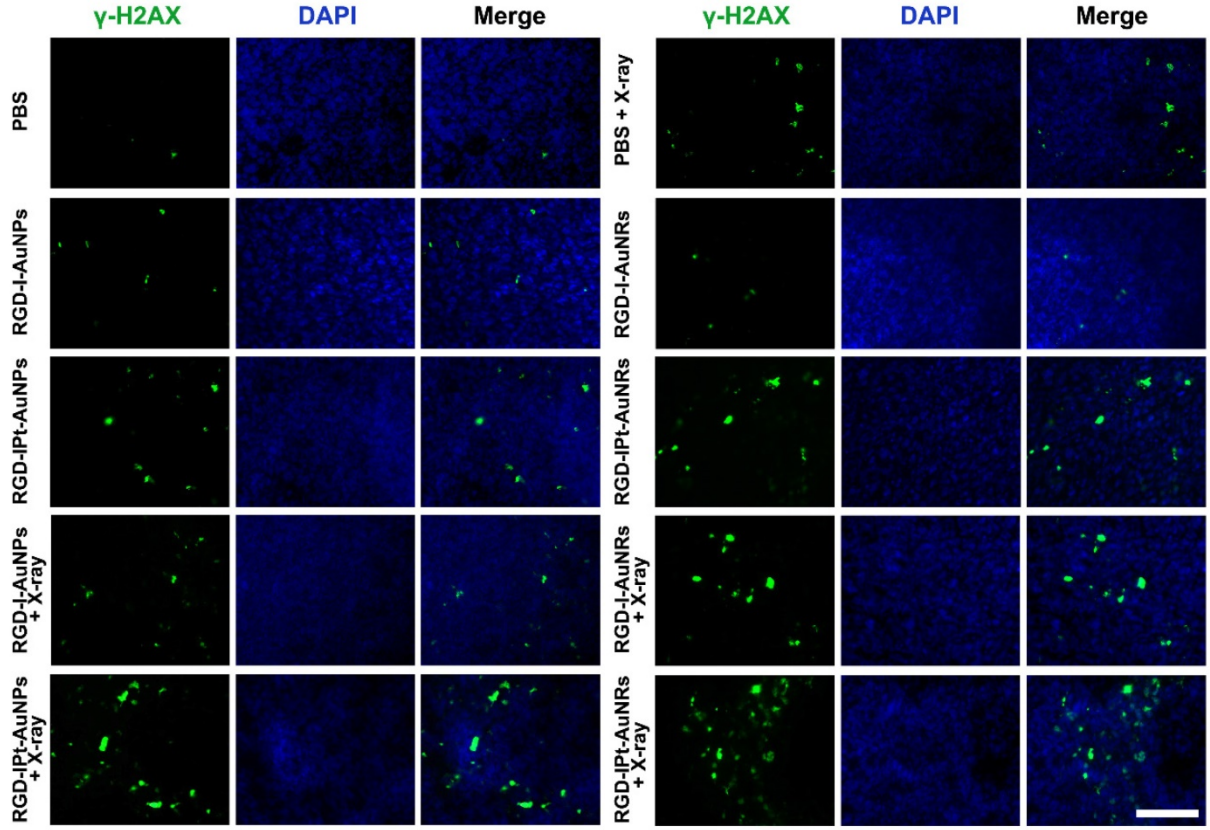


**Figure 7.** γ-H2AX immunostaining images of tumor tissues two days after the treatments. The mice were treated with either RGD-IPt-AuNPs or RGD-IPt- AuNRs in combination with 6 Gy of X-ray radiation. Scale bar: 100 μm.

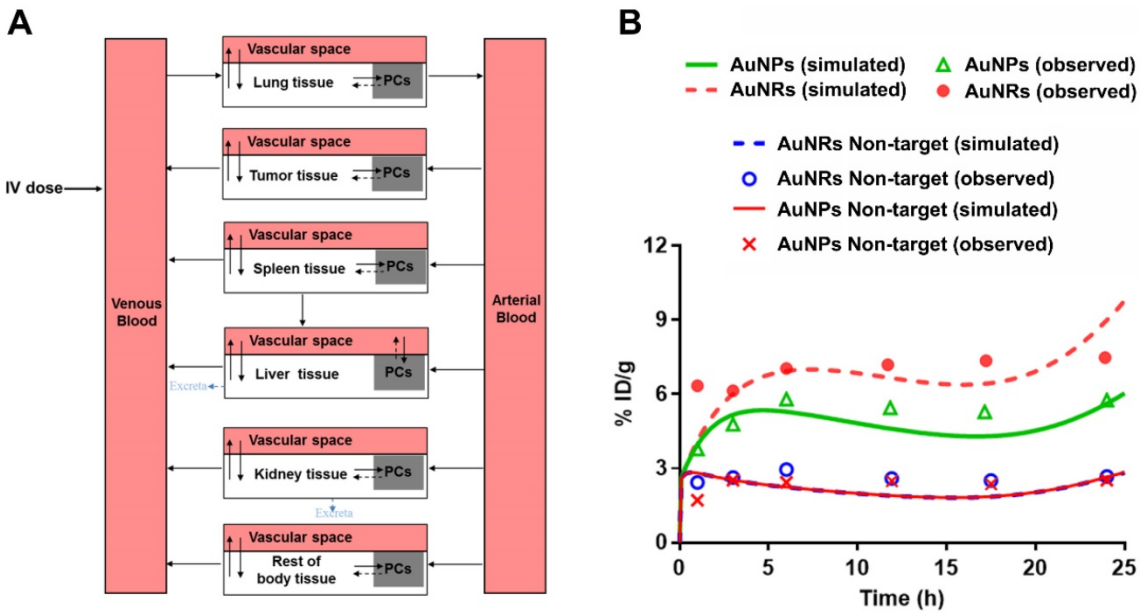


**Figure 8.** *In vivo* kinetics of AuNPs and AuNRs probes. (A) Schematic diagram of the mathematical compartment model. Gray boxes indicate the NPs uptake by phagocytic cells isolated from blood circulation or tissues. (B) Model calibration results with experimental data. The line represents the concentration-time profile of probes simulated by the model.

As shown in Figure S9, the time profiles of probe concentration observed in major organs of mice were adequately described by the developed mathematical model with an overall regression coefficient ($R^2$) of 0.92. Non-targeting AuNRs (GNR NT) displayed a much higher tumor accumulation than non-targeting AuNPs (GNP NT) at 1 h post-injection (2.43 *vs* 1.71 ID% mL, $p < 0.05$, Figure 8B). However, similar tumor accumulations were observed for both types of non-targeting probes at 24 h post-injection (2.52 *vs* 2.67 ID%/mL), indicating that the shapes of NPs did not have a high influence on their tumor accumulations through EPR effect in long term. For RGD-conjugated target NPs, the distribution coefficients ($P$) and the maximum uptake rate constant ($K_{max}$) were determined to be higher for RGD-$^{125}$IPt-AuNRs than RGD-$^{125}$IPt-AuNPs (0.25 *vs* 0.15; 20 $h^{-1}$ *vs* 10 $h^{-1}$), indicating the more rapid distribution of RGD-$^{125}$IPt-AuNRs into tumor interstitial fluid and the higher ingestion of RGD-$^{125}$IPt-AuNRs by tumor cells, while other parameters of these two probes were the same (Table S5).

## Discussion

Gold NPs have been extensively explored for tumor theranostics [47] and the key factor governing the performances is the tumor accumulation efficiency of NPs. Therefore, *in vivo* behaviors of gold NPs with different configurations and formulations have been intensively studied to obtain the maximal tumor accumulation [48]. In this study, RGD peptide-conjugated, cisplatin-loaded, $^{125}$I-labeled, spherical (RGD-$^{125}$IPt-AuNPs) and rod-shaped (RGD-$^{125}$IPt-AuNRs) gold nano theranostic probes have been developed. By using a H1299 tumor model, we were able to evaluate the shape-effect of active targeting NPs on tumor accumulation efficiency and thus the tumor therapeutic efficacy by chemo-radiotherapy when NPs simultaneously targeting tumor neovesculatures and cells along with EPR effect, which was different from previous reports considering the shape effect on tumor accumulation through either EPR effect or active targeting by addressing tumor cells.

Tumor accumulation of NPs was influenced by extravasation, intra-tumoral diffusion and interaction of NPs with tumor cells. The particle size, morphology and surface properties are key parameters affecting their extravasation, intra-tumoral diffusion and retention [16, 49]. In our study, both real-time observations and simulation by the PBPK model revealed that tumor accumulations of the non-targeting, rod-shaped RAD-$^{125}$IPt- AuNRs through EPR effect were more efficient than those of the spherical RAD-$^{125}$IPt-AuNPs in short-term (1h post-injection), being consistent with previous reports [16, 20]. However, the tumor accumulations of both particles were similar in long-term (24 h post-injection). For RGD probes, however, tumor accumulation of the rod-shaped RGD-$^{125}$IPt-AuNRs was significantly more than the spherical RGD-$^{125}$IPt-AuNPs at each time point. PBPK simulation-derived estimates of the distribution coefficients ($P$), a parameter reflecting distribution of NPs into interstitial fluid, was much higher for rod-shaped RGD-$^{125}$IPt-AuNRs than spherical RGD-$^{125}$IPt-AuNPs.

The simulation results could be validated by previous observations. Chauhan *et al* have tested tumor penetration efficiency of fluorescent nanorods and nanospheres using multiphoton microscopy within the same tumor, and found that the nanorods penetrated into tumors 4.1 times as rapidly as the nanospheres [50]. Moreover, the rod-shaped RGD-$^{125}$IPt-AuNRs penetrated deeper into tumor interstitials than the spherical one, as revealed by silver staining of tumor tissues. Our findings were consistent with previous studies on intra-tumoral distributions of radioactive $^{198}$Au nanostructures by autoradiographic imaging, which revealed that the AuNPs were only distributed on the surfaces of tumors, while the AuNRs were observed throughout tumors [51]. In addition, the maximum uptake rate constant ($K_{max}$) of RGD-$^{125}$IPt-AuNRs, a parameter indicating tumor cell uptake of NPs, was 2 times higher than RGD-$^{125}$IPt-AuNPs. The differential effects of NP shape on tumor accumulations through EPR effect and active targeting might be explained by the fact that although AuNRs diffuses faster and deeper than AuNPs in tumor interstitials, high intra tumor pressure induced by impaired lymphatic drainage would induce intravasation of NPs into blood vessels if they could not anchor the tumor cells [52]. As revealed by *in vitro* studies, the RGD probes were able to specifically target to $\alpha v\beta 3$ positive tumor cells, with the rod-shaped RGD-$^{125}$IPt-AuNRs had more efficient targeting than RAD probes. Moreover, compared to its spherical counterpart, RGD-$^{125}$IPt-AuNRs had a longer blood half-life because the rod-shaped materials tend to evade phagocytosis and clearance by macrophages in blood and reticuloendothelial system [53, 54]. Longer blood half-life means NPs have the more chance to permeate into tumor interstitials and address tumor cells. These rod shape-related, favorable factors could contribute to higher tumor accumulation of RGD-$^{125}$IPt-AuNRs. These results indicated that the morphology affected both *in vivo* and intra-tumor kinetics of gold nanoprobes, and NP shape and active targeting ligands are important for efficient tumor accumulation. However, we did not find the significant difference of distribution patterns of these two types of probes in the other major organs such as the liver and spleen.

In addition to high tumor accumulation, the rod-shaped NPs were also found to be more efficient for cisplatin loading. Under alkaline conditions, dopamine is able to self-polymerize and spontaneously deposit on the surface of almost any material [55]. Lots of functional groups, such as carboxyl , quinone functions and catechol, might be included in the PDA layer, which may provide a versatile platform for drug loading and surface modifications with functionalities [56]. We loaded cisplatin onto PDA-coated gold NPs by hydrating cisplatin into $[Pt(H_2O)_2(NH_2)_2]^{2+}$, which could chelate the catechol groups in PDA [32]. As demonstrated previously, the PDA coating layer was thin (around 1~2 nm in thickness) and uniform, and the drug loading efficiency was determined by the PDA coating area. Because the surface area of AuNRs is much larger than that of AuNPs in the same mass ($5.52 \times 10^{17}$ *vs* $2.85 \times 10^{17}$ nm$^2$ per milligram), it is conceivable that RGD-$^{125}$IPt-AuNRs had a much higher loading efficiency for cisplatin than RGD-$^{125}$IPt-AuNPs.

Angiogenesis is very important for tumor growth and metastasis [57]. Targeting tumor angiogenesis through the highly expressed $\alpha v\beta 3$ integrin has been approved as an effective way for tumor therapy [58]. In our study, as revealed by high resolution PAI, both RGD-IPt-AuNPs and RGD-IPt-AuNRs were able to localize tumor neovasculatures, with the rod-like probes being more effective. By releasing the chemo drug and localizing radiation damage directly to the tumor-associated endothelial cells, the tumor neovesculatures would be damaged and unable to transport nutrients to tumor tissues, inducing ischemic necrosis of tumor. Although both types of RGD probes could also address tumor cells as indicated by silver staining, the nutrients supply inhibited mechanism for tumor suppression may be more effective than tumor clonogenic cells death itself [59].

## Conclusions

In conclusion, both RGD-$^{125}$IPt-AuNPs and RGD-$^{125}$IPt-AuNRs were able to target tumor cells and angiogenic vessels. Compared to the spherical RGD-$^{125}$IPt-AuNPs, the rod-shaped RGD-$^{125}$IPt-AuNRs have a higher drug loading efficiency, more rapid diffusion in and deep penetration into tumor interstitials, higher specificity for $\alpha v\beta 3$ integrin and thus more efficient tumor accumulation. Therefore, RGD-$^{125}$IPt-AuNRs have more antitumor efficacy for chemotherapy and chemo-radiotherapy. Our study suggests that gold NPs' shapes and targeting ligands are both important in tumor accumulation and chemo-radiotherapy.

## Experimental

### Materials

All the chemical reagents were purchased from Sinopharm Chemical Regent Col Ltd (Shanghai, China) unless indicated otherwise. All the glass containers used in experiments were cleaned by aqua regia, washed extensively with ultrapure water (Milli Q Integral 5 system).

### Synthesis of Gold Nanospheres (AuNPs) and Nanorods (AuNRs)

AuNPs were synthesized according to the previous report [60]. In brief, gold nano seeds were first synthesized by direct reduction of $HAuCl_4$ by $NaBH_4$ in the presence of trisodium citrate dihydrate. Then, 200 μL of seeds solution was injected into a growth solution quickly and allowed for growth for 10 min. Afterwards, the particles were retrieved, rinsed and then kept in water for next procedure.

AuNRs were synthesized according to our previous report [61]. The as-synthesized AuNRs were coated by CTAB in situ and dispersed in deionized water.

The numbers of AuNPs and AuNRs per milligram were calculated. Herein, AuNPs are assumed as a perfect sphere, and the volume of one AuNP ($V_{AuNP}$) is calculated by

$$V_{AuNP} = \frac{1}{6}\pi R^3 \quad (1)$$

Where R is the diameter of AuNPs.

AuNRs are assumed as a cylinder with two hemispherical caps [62], and the volume of an individual AuNR ($V_{AuNR}$) can be calculated by

$$V_{AuNR} = \frac{\pi D^3}{8}\left[\frac{4}{3} + 2\,(Y-1)\right] \quad (2)$$

Here, Y is the aspect ratio of AuNRs and equals to L/D, D and L are the diameter and length of the AuNRs, respectively.

The weight of an individual AuNP and AuNR can be determined by M = ρV, in which ρ and V are density of gold and volume of a gold NP, respectively.

The amount of AuNPs ($m_{AuNPs}$) per milligram is calculated by

$$m_{AuNPs} = \frac{V}{V_{AuNPs}} = \frac{6M}{\pi\rho R^3} \quad (3)$$

and the amount of AuNRs ($m_{AuNRs}$) in one milligram is calculated by the following formula:

$$m_{AuNRs} = \frac{V}{V_{AuNRs}} = \frac{8M}{\pi D^3\left[\frac{4}{3}+2\,(Y-1)\right]\rho} \quad (4)$$

### Preparation of RGD-$^{125}$IPt-AuNPs and RGD-$^{125}$IPt-AuNRs Probes

Both the spherical and rod-shaped probes were prepared by five steps: poly dopamine (PDA) surface coating, PEG modification, RGD peptide conjugation, cisplatin loading and iodine-125 labeling. The detailed synthesis procedure referred to our previous report [27].

### Characterization

Zeta-potentials of AuNPs and AuNRs during the probe preparation were measured by Malvern Zetasizer Nano ZSP instrument (Malvern, Britain). The morphology, EDS element mapping images were obtained by using TEM (JEOL, Japan) operating at 200 kV acceleration voltage. Probe size distributions were analyzed using ImageJ software by measuring the diameters of ≥ 200 particles. The optical properties and the stability of both types of NPs and probes in physiological conditions (RPMI-1640 culture medium plus 10% FBS) were evaluated by examining their UV–VIS spectra (Cary 50 Bio, Varian, USA) at different time point (30 min, 3, 6, 24, 72 h). The Ellman method was used to evaluate the efficiency of PEG modification and peptide conjugation [30]. Accordingly, the amount of PEG molecules and RGD peptides anchored on an individual particle were able to be calculated.

### Drug Release

The cisplatin release profile was studied by suspending RGD-IPt- AuNPs or RGD-IPt-AuNRs (10 mg) into PBS (20 mL) in dialysis tubes (800 Da MWCO) and dialyzed against plain PBS at 37 °C. One milliliter of dialysis solution was removed at different time intervals and replenished by fresh corresponding buffer. The detached cisplatin was measured by atomic absorption spectroscopy (AAS, Hitachi, Japan).

### Cell Culture

A human lung cancer H1299 cells line was obtained from cell bank of Chinese Academy of Sciences (Shanghai, China) and cultured in RPMI-1640 culture medium (Invitrogen, California, USA) containing glucose 2.5 g/L, $NaHCO_3$ 1.5g/L, and Sodium Pyruvate 0.11g/L, and supplemented with 10% FBS (Invitrogen, California, USA) under 5% $CO_2$ at 37 °C. The H1299 cells were re-seeded in 6-well plates at a population of $5\times10^5$ cells per well 24 h before experiments.

### Specificity of RGD-probes for $\alpha v\beta 3$ Integrin

H1299 cells were disseminated on cover slices and cultured with media containing RGD, RAD-probes (50 μg Au /mL) or RGD probes + free RGD peptide (10 μM, defined as competition groups) for 1 h in 6-well plates. Subsequently, the culture media were removed. The cells were then washed with PBS, fixed with 4% paraformaldehyde and stained by DAPI sequentially. The cells were imaged by two-photo fluorescence microscopy (A1plus, Nikon, Japan) and the horizontal z-stack images were captured at a distance of 0.25 μm between each two slices along the *z*-axis. Moreover, the intracellular contents of gold element were also quantified by AAS. Triplet experiments were conducted and the intracellular gold content was indicated as mean ± SD in pictograms of gold element per cell.

### Chemotherapy on Tumor Cells

Chemotherapeutic effect of the probes on tumor cells was examined by treating H1299 cells with RGD-IPt-AuNPs or RGD-IPt-AuNRs at different concentrations (10, 25, 50, and 100 μg Au /mL) for 6, 24 or 48 h, using drug-free probes as controls. The cell viability was assayed by CCK-8 assay (Beyotime Biotechnology, Shanghai, China) [63]. For immunofluorescence staining, the cells were treated with 50 μg Au /mL of probes for 48 h, fixed by paraformaldehyde, and then incubated with anti-γ-H2AX primary antibody (1:250, Invitrogen) and Alexa-488 conjugated secondary antibody (1: 400, Invitrogen) sequentially. After co-staining with DAPI, the immunofluorescence images of the treated cells were obtained by inverted fluorescence microscope (Leica, Germany).

### Chemo-radiotherapy on Tumor Cells

For chemo-radiotherapy of the probes on tumor cells, H1299 cells were first treated with RGD-IPt-AuNPs or RGD-IPt-AuNRs at 50 μg Au /mL for 6 h, and then irradiated by X-ray (320 kV, Precision X-Ray, North Branford, CT) for a dosage of 4 Gy. The viability of the treated cells was examined by using CCK-8 assay during the next 4 days [5].

To calculate the combination index (CI) of chemo-radiotherapy by using the probes, the cells were incubated with both types of probes at different concentrations (10, 25, 50, 100 μg Au /mL) for 6 h and then irradiated by X-ray for a dosage of 4 Gy. Cell viability was then examined. The combination indexes of chemo-radiotherapy were calculated by using the formula as below:

$$\mathrm{CI} = \frac{C_1}{C_{x1}} + \frac{C_2}{C_{x2}} \quad (5)$$

Where $C_1$ and $C_2$ are the concentration of RGD-IPt-AuNPs or RGD-IPt-AuNRs to achieve a certain effect in chemo-radiotherapy, and $C_{x1}$ and $C_{x2}$ are the concentrations of RGD-IPt-AuNPs or RGD-IPt-AuNRs and the drug free probes (RGD-I-AuNPs or RGD-I-AuNRs) with radiotherapy that obtain equal effect alone [64]. CI < 1, = 1, or > 1, chemotherapy and radiotherapy are indicated to have synergistic, additive, or antagonistic effects, respectively. Here, we chose the 75 % of cell viability as the equal therapeutic effect and using IBM SPSS statistics 19.0 (IBM, New York, USA) to calculate the certain relative concentration of all types of probes.

### SPECT/CT Imaging and Bio-distribution Studies

All the animal experiments were carried out complying with the guidelines of Animal Protection and Care Committee of Shanghai Jiao Tong University. H1299 tumor xenograft models were first prepared. Briefly, H1299 cells ($3 \times 10^6$ cell/site) suspended in 200 μL of serum-free RPMI-1640 were subcutaneously inoculated into the right flank of nude mice (Balb/c, 20 g, Slaccas, China). After 2-3 weeks of inoculation, the size of the tumors reached around 5 mm, and the mice were then used for follow-up experiments. For SPECT/CT imaging, the tumor-bearing mice were administered with RGD or RAD probes (0.15 mL, 300 μCi) intravenously. Competition studies were conducted by injection of RGD peptide conjugated probes plus free RGD peptides (10 mM, 0.1mL). SPECT/CT scans were performed by using a small-animal SPECT/CT scanner (Nano SPECT/CT® PLUS, Bioscan, USA). For bio-distribution study, the mice (three mice in each group) were intravenously injected with the probes at the conditions exactly same as that for SEPCT/CT scanning. The mice were euthanized at different time points after probe injection, and the samples of main organs (heart, lungs, kidney, spleen, liver, intestine, stomach, and muscle), blood and tumors were obtained, weighed, and countered by well-type scintillation detector. The counters were transferred into radioactivity. Accordingly, the percentage of injected dose per gram of tissue (%ID/g) was obtained [65].

### Evaluation of Probe Blood Half-life

Mice with H1299 tumor (five mice in each group) were administered intravenously with 200 μL, 100 μCi of PEG-$^{125}$IPt-AuNRs, PEG-$^{125}$IPt-AuNPs, RAD-$^{125}$IPt-AuNRs, RAD-$^{125}$IPt-AuNPs, RGD-$^{125}$IPt-AuNRs or RGD-$^{125}$IPt-AuNPs. The blood samples were collected at 10, 15, 20, 30, 60, 120, 240 and 360 min post-injection from the tail vein, and countered in a well-type scintillation detector. By using Berkeley Madonna software (version 8.3.18, Berkeley, CA, USA), blood half-lives of probes in %ID/g were fitted with the two-compartment bolus intravenous injection model [66, 67].

### Photoacoustic Imaging

In photoacoustic imaging process, a confocal optical high-resolution photoacoustic microscopy (OR-PAM) was utilized [41]. Briefly, the animal was anesthetized by isoflurane and fixed in a custom-built holder. A two-dimensional translation stage drove the OR-PAM imaging head to realize imaging by implementing a raster scan. To guarantee minimal interference from animal displacement, the animal was maintained in its original position until all PA MAP images were acquired. The light source for the system is a pulsed dye laser (DL-10-5, Elforlight). The repetition rate was 5 kHz in imaging. The imaging wavelength was 532 nm, at which the hemoglobin, AuNPs and AuNRs have optical absorption. After

imaging, maximum amplitude projection (MAP) image was obtained by projecting the maximum signal amplitude in each depth-resolved one-dimensional PA signal onto the transverse plane. MAP images were acquired before injection and at 1, 4, 24 h after injection.

The mice were euthanatized after PA imaging. The tumors were obtained and the tumor tissues were processed for immunohistochemical (IHC) staining against tumor vessels (CD31) and $\alpha v\beta 3$ integrin (CD 61) and silver staining against the probes (gold) according to our previous reports [26].

### Chemo-radiotherapy *in vivo* and Histological Studies

To evaluate the chemo-radiotherapy effect of the probes, mice with H1299 tumors (around 50 $mm^3$ in volume) were treated with both types of RGD probes for chemotherapy only (40 mg Au/kg in body weight) or the probes plus 6 Gy of X-ray irradiation (320 kV, Precision X-Ray, North Branford, CT) for chemo-radiotherapy 6 h post probe injection. All the treatments were done only once. After the treatments, the tumor sizes were measured and the tumor volumes (V, $mm^3$) were calculated according to formula $V = 3\pi lw^2/4$ [68], in which w and l were the width and length of the tumor. Tumor growth was indicated by $V/V_0$, where$V_0$ is the tumor volume before treatment.

To assess the therapeutic effect histologically, three mice from each group were sacrificed two days after the treatments, and tumors were removed and processed for IHC studies against γ-H2AX following the same procedure for cell staining. Moreover, 21 days after the treatments, all the treated mice were sacrificed. The major organs (heart, spleen, liver, kidney and lung) were obtained, and processed for hematoxylin/eosin staining to evaluate the biocompatibility of probes [26, 27].

### Statistics

All experiment data expressed are the calculated mean ± standard deviation (SD). A student's t test was used for differences of statistically significant evaluation, and $p < 0.05$ was regarded as significant differences between groups.

### Compartment Modeling of Suborgan Kinetics of AuNPs and AuNRs

The mass balance equation for each organ compartment is described as below:

$$\frac{dA_{blood}}{dt} = Q \times C_a - Q \times \frac{A_{blood}}{V_{vas}} - k_{up} \times A_{blood} + k_{re} \times A_{tissue} \quad (6)$$

$$\frac{dA_{tissue}}{dt} = k_{up} \times A_{blood} - k_{re} \times A_{tissue} \quad (7)$$

$$C_k = \frac{A_{blood}+A_{tissue}}{V_k} \quad (8)$$

Where $A_{blood}$ is the amount of NPs in the organ blood sub-compartment, $A_{tissue}$ is amount of NPs in the organ tissue sub-compartment, $Q$ is blood flow to the organ, $V_{vas}$ is blood volume of the organ, $V_k$ is total organ volume, $C_a$ is concentration of NP in the artery, $k_{up}$ is the uptake rate constant, $k_{re}$ is the release rate constant, and $C_k$ is the concentration of NPs in organ. The physiological parameters ($V_{vas}$,$Q$, $V_k$) were according to the mouse bodyweight [69]. As NPs were gradually taken up by tumor cells, $k_{up}$ was assumed to be time-dependant and can be described by a Hill equation as below:

$$k_{up} = \frac{K_{max} \times T^n}{{T_{50}}^n \times T^n} \quad (9)$$

Where $K_{max}$ is the maximum uptake rate constant, $T$ is the time, $T_{50}$ is the time to reach half of $K_{max}$, and n is the Hill coefficient. These NP dependent parameters were determined by curve fitting of the time profile of NP concentration in organs. Compartment modeling was carried out using Berkeley Madonna version 8.3.18 (Berkeley, CA, USA).

## Acknowledgements

This work was supported by grants from NSFC (81571729 and 81772338, to C. Zhang), SJTU (YG2017ZD05, to C. Zhang), Innovation Research Plan supported by Shanghai Municipal Education Commission (ZXWF082101, to C. Zhang), and Australian National Health and Medical Research Council (APP 1141121, to H. Wang).

## Supplementary Material

Supplementary figures and tables.
http://www.thno.org/v09p1893s1.pdf
Supplementary 2.
http://www.thno.org/v09p1893s2.pdf
Supplementary 3.
http://www.thno.org/v09p1893s3.pdf

## Competing Interests

The authors have declared that no competing interest exists.

## References

1. Seiwert TY, Salama JK, Vokes EE. The concurrent chemoradiation paradigm-general principles. Nat Clin Pract Oncol. 2007; 4: 86-100.
2. Begg AC, Stewart FA, Vens C. Strategies to improve radiotherapy with targeted drugs. Nat Rev Cancer. 2011; 11: 239-53.
3. Liu H, Xie Y, Zhang Y, Cai Y, Li B, Mao H, et al. Development of a hypoxia-triggered and hypoxic radiosensitized liposome as a doxorubicin carrier to promote synergetic chemo-/radio-therapy for glioma. Biomaterials. 2017; 121: 130-43.

4. Chen S, Lin L, Kuo Y, Liang JA, Kuo CC, Chiou JF. Phase 2 study of combined sorafenib and radiation therapy in patients with advanced hepatocellular carcinoma. Int J Radiat Oncol Biol Phys. 2014; 88: 1041-7.
5. Fan W, Shen B, Bu W, Chen F, Zhao K, Zhang S, et al. Rattle-structured multifunctional nanotheranostics for synergetic chemo-radiotherapy and simultaneous magnetic/luminescent dual-mode imaging. J Am Chem Soc. 2013; 135: 6494-503.
6. Zhang H, Li L, Liu X, Jiao J, Ng C, Yi J, et al. Ultrasmall ferrite nanoparticles synthesized via dynamic simultaneous thermal decomposition for high-performance and multifunctional T1 magnetic resonance imaging contrast agent. ACS Nano. 2017; 11: 3614-31.
7. Song G, Cheng L, Chao Y, Yang K, Liu Z. Emerging nanotechnology and advanced materials for cancer radiation therapy. Adv Mater. 2017; 29: 1700996
8. Fan W, Yung B, Huang P, Chen X. Nanotechnology for multimodal synergistic cancer therapy. Chem Rev. 2017; 117: 13566-638.
9. Yang X, Yang M, Pang B, Vara M, Xia Y. Gold Nanomaterials at work in biomedicine. Chem Rev. 2015; 115: 10410-88.
10. Chithrani BD, Jelveh S, Jalali F, van Prooijen M, Allen C, Bristow RG, et al. Gold nanoparticles as radiation sensitizers in cancer therapy. Radiat Res. 2010; 173: 719-28.
11. Retif P, Pinel S, Toussaint M, Frochot C, Chouikrat R, Bastogne T, et al. Nanoparticles for radiation therapy enhancement: the key parameters. Theranostics. 2015; 5: 1030-44.
12. Cui L, Her S, Borst GR, Bristow RG, Jaffray DA, Allen C. Radiosensitization by gold nanoparticles: will they ever make it to the clinic?. Radiother Oncol. 2017; 124: 344-56.
13. Her S, Jaffray DA, Allen C. Gold nanoparticles for applications in cancer radiotherapy: mechanisms and recent advancements. Adv Drug Deliv Rev. 2017; 109: 84-101.
14. Ma N, Jiang Y, Zhang X, Wu H, Myers JN, Liu P, et al. Enhanced radiosensitization of gold nanospikes via hyperthermia in combined cancer radiation and photothermal therapy. ACS Appl Mater Interfaces. 2016; 8: 28480-94
15. Ma N, Liu P, He N, Gu N, Wu F, Chen Z, et al. Action of gold nanospikes-based nanoradiosensitizers: cellular internalization, radiotherapy, and autophagy. ACS Appl Mater Interfaces. 2017; 9: 31526-42
16. Arnida, Janát-Amsbury MM, Ray A, Peterson CM, Ghandehari H. Geometry and surface characteristics of gold nanoparticles influence their biodistribution and uptake by macrophages. Eur J Pharm Biopharm. 2011; 77: 417-23.
17. Perry JL, Reuter KG, Luft JC, Pecot CV, Zamboni W, DeSimone JM. Mediating passive tumor accumulation through particle size, tumor type, and location. Nano Lett. 2017; 17: 2879-86.
18. Tong X, Wang Z, Sun X, Song J, Jacobson O, Niu G, et al. Size dependent kinetics of gold nanorods in EPR mediated tumor delivery. Theranostics. 2016; 6: 2039-51.
19. Zhang X, Wu D, Shen X, Chen J, Sun Y, Liu P, et al. Size-dependent radiosensitization of PEG-coated gold nanoparticles for cancer radiation therapy. Biomaterials. 2012; 33: 6408-19.
20. Wang Y, Black KCL, Luehmann H, Li W, Zhang Y, Cai X, et al. Comparison study of gold nanohexapods, nanorods, and nanocages for photothermal cancer treatment. ACS Nano. 2013; 7: 2068-77.
21. Wilhelm S, Tavares AJ, Dai Q, Ohta S, Audet J, Dvorak HF, et al. Analysis of nanoparticle delivery to tumours. Nat Rev Mater. 2016; 1: 16014-26.
22. England CG, Gobin AM, Frieboes HB. Evaluation of uptake and distribution of gold nanoparticles in solid tumors. Eur Phys J Plus. 2015; 130: 231-47.
23. Jain RK, Stylianopoulos T. Delivering nanomedicine to solid tumors. Nat Rev Clin Oncol. 2010; 7: 652-64.
24. Li R, Zheng K, Yuan C, Chen Z, Huang M. Be active or not : the relative contribution of active and passive tumor targeting of nanomaterials. Nanotheranostics. 2017; 1: 346-57.
25. Bertrand N, Wu J, Xu X, Kamaly N, Farokhzad OC. Cancer nanotechnology: the impact of passive and active targeting in the era of modern cancer biology. Adv Drug Deliv Rev. 2014; 66: 2-25.
26. Yang Y, Zhang L, Cai J, Li X, Cheng D, Su H, et al. Tumor angiogenesis targeted radiosensitization therapy using gold nanoprobes guided by MRI/SPECT imaging. ACS Appl Mater Interfaces. 2016; 8: 1718-32.
27. Zhang L, Su H, Cai J, Cheng D, Ma Y, Zhang J, et al. A multifunctional platform for tumor angiogenesis-targeted chemo-thermal therapy using polydopamine-coated gold nanorods. ACS Nano. 2016; 10: 10404-17.
28. Lynge ME, Schattling P, Städler B. Recent developments in poly ( dopamine ) - based coatings for biomedical applications. Nanomedicine (Lond). 2015; 10: 2725-42.
29. Perrault SD, Walkey C, Jennings T, Fischer HC, Chan W. Mediating tumor targeting efficiency of nanoparticles through design. Nano Lett. 2009; 9: 1909-15.
30. Ellman GL. Tissue sulfhydryl groups. Arch Biochem Biophys. 1959; 82: 70-7.
31. Hu M. Measurement of protein thiol groups and glutathione in plasma. Methods Enzymol. 1994; 233: 380-5.
32. Fan Q, Cheng K, Hu X, Ma X, Zhang R, Yang M, et al. Transferring biomarker into molecular probe: melanin nanoparticle as a naturally active platform for multimodality imaging. J Am Chem Soc. 2014; 136: 15185-94.
33. Irigoyen M, Pajares MJ, Agorreta J, Ponz-Sarvisé M, Salvo E, Lozano MD, et al. TGFBI expression is associated with a better response to chemotherapy in NSCLC. Mol Cancer. 2010; 9: 130-42.
34. Kiessling F, Huppert J, Zhang C, Jayapaul J, Zwick S, Woenne EC et al. RGD-labeled USPIO inhibits adhesion and endocytotic activity of αvβ3-integrin–expressing glioma cells and only accumulates in the vascular tumor compartment. Radiology. 2009; 253: 462-9.
35. Zhang C, Xie X, Liang S, Li M, Liu Y, Gu H. Mono-dispersed high magnetic resonance sensitive magnetite nanocluster probe for detection of nascent tumors by magnetic resonance molecular imaging. Nanomedicine: NBM. 2012; 8: 996-1006.
36. Ma N, Wu F, Zhang X, Jiang Y, Jia H, Wang H, et al. Shape-dependent radiosensitization effect of gold nanostructures in cancer radiotherapy: comparison of gold nanoparticles, nanospikes, and nanorods. ACS Appl Mater Interfaces. 2017; 9: 13037-48.
37. Yu M, Zheng J. Clearance pathways and tumor targeting of imaging nanoparticles. ACS Nano. 2015; 9: 6655-74.
38. Wen L, Chen L, Zheng S, Zeng J, Duan G, Wang Y, et al. Ultrasmall biocompatible $WO_{3-x}$ nanodots for multi-modality imaging and combined therapy of cancers. Adv Mater. 2016; 28: 5072-9.
39. Mizejewski GJ. Role of integrins in cancer: survey of expression patterns. Proc Soc Exp Biol Med. 1999; 22: 124-38.
40. Brooks P, Clarck R, Cheresh D. Requirement of vascular integrin alpha(V)beta(3) for angiogenesis. Science. 1994; 264: 569-71.
41. Li Q, Li L, Yu T, Zhao Q, Zhou C, Chai X. Vascular tree extraction for photoacoustic microscopy and imaging of cat primary visual cortex. J Biophotonics. 2016; 12: 780-91.
42. Wang Z, Shao D, Chang Z, Lu M, Wang Y, Yue J, et al. Janus gold nanoplatform for synergetic chemoradiotherapy and computed tomography imaging of hepatocellular carcinoma. ACS Nano. 2017; 11: 12732-41.
43. Chen Y, Song G, Dong Z, Yi X, Chao Y, Liang C, et al. Drug-loaded mesoporous tantalum oxide nanoparticles for enhanced synergetic chemoradiotherapy with reduced systemic toxicity. Small. 2017; 13: 1602869.
44. Setua S, Ouberai M, Piccirillo SG, Watts C, Welland M. Cisplatin-tethered gold nanospheres for multimodal chemo-radiotherapy of glioblastoma. Nanoscale. 2014; 6: 10865-73.
45. Liang X, Wang H, Grice JE, Li L, Liu X, Xu ZP, et al. Physiologically based pharmacokinetic model for long-circulating inorganic nanoparticles. Nano Lett. 2016; 16: 939-45.
46. Lin Z, Monteiro-Riviere NA, Riviere JE. A physiologically based pharmacokinetic model for polyethylene glycol-coated gold nanoparticles of different sizes in adult mice. Nanotoxicology. 2016; 10: 162-72.
47. Cabral RM, Baptista PV. Anti-cancer precision theranostics: a focus on multifunctional gold nanoparticles. Expert Rev Mol Diagn. 2014; 14: 1041-52.
48. Sykes EA, Chen J, Zheng G, Chan W. Investigating the impact of nanoparticle size on active and passive tumor targeting efficiency. ACS Nano. 2014; 8: 5696-706.
49. Frellsen AF, Hansen AE, Jølck RI, Kempen PJ, Severin GW, Rasmussen PH, et al. Mouse positron emission tomography study of the biodistribution of gold nanoparticles with different surface coatings using embedded copper-64. ACS Nano. 2016;10: 9887-98.
50. Chauhan VP, Popovic Z, Chen O, Cui J, Fukumura D, Bawendi MG, et al. Fluorescent nanorods and nanospheres for real-time in vivo probing of nanoparticle shape-dependent tumor penetration. Angew Chem Int Ed Engl. 2011; 50: 11417-20.
51. Black KCL, Wang Y, Luehmann HP, Cai X, Xing W, Pang B, et al. Radioactive 198Au-Doped Nanostructures with Different Shapes for in Vivo Analyses of Their Biodistribution, Tumor Uptake, and Intratumoral Distribution. ACS Nano. 2014; 8: 4385-94.
52. Adams GP, Schier R, McCall AM, Simmons HH, Horak EM, Alpaugh RK, et al. High affinity restricts the localization and tumor penetration of single-chain Fv antibody molecules. Cancer Res. 2001; 61: 4750-5.
53. Champion JA, Mitragotri S. Role of target geometry in phagocytosis. Proc Natl Acad Sci U S A. 2006; 103: 4930-34.
54. Geng Y, Dalhaimer P, Cai SS, Tsai R, Tewari M, Minko T, et al. Shape effects of filaments versus spherical particles in flow and drug deliver. Nat Nanotechnol. 2007; 2: 249-55.
55. Liu Y, Ai K, Lu L. Polydopamine and its derivative materials: synthesis and promising applications in energy, environmental, and biomedical fields. Chem Rev. 2014; 114: 5057-115.
56. Lee H, Dellatore SM, Miller WM, Messersmith PB. Mussel-ispired surface chemistry for multifunctional coating. Science. 2007; 318: 426-30.
57. Carmeliet P, Jain RK. Angiogenesis in cancer and other diseases. Nature. 2000; 407: 249-57.
58. Kunjachan S, Pola R, Gremse F, Theek B, Ehling J, Moeckel D, et al. Passive versus active tumor targeting using RGD- and NGR-modified polymeric nanomedicines. Nano Lett. 2014; 14: 972-81.
59. Garcia-Barros M, Paris F, Cordon-Cardo C, Lyden D, Rafii S, Haimovitz-Friedman A, et al. Tumor response to radiotherapy regulated by endothelial cell apoptosis. Science. 2003; 300: 1155-9.
60. Gao C, Vuong J, Zhang Q, Liu Y, Yin Y. One-step seeded growth of Au nanoparticles with widely tunable sizes. Nanoscale. 2012; 4: 2875-8.
61. Ye X, Zheng C, Chen J, Gao Y, Murray CB. Using binary surfactant mixtures to simultaneously improve the dimensional tunability and monodispersity in the seeded growth of gold nanorods. Nano Lett. 2013; 13: 765-71.
62. Edgar JA, McDonagh AM, Cortie MB. Formation of gold nanorods by a stochastic "popcorn" mechanism. ACS Nano. 2012; 6: 1116-25.

63. Zhang L, Wang Y, Tang Y, Jiao Z, Xie C, Zhang H, et al. High MRI performance fluorescent mesoporous silica-coated magnetic nanoparticles for tracking neural progenitor cells in an ischemic mouse model. Nanoscale. 2013; 5: 4506-16.
64. Yang J, Su H, Sun W, Cai J, Liu S, Chai Y et al. Dual chemodrug-loaded single-walled carbon nanohorns for multimodal imaging-guided chemo-photothermal therapy of tumors and lung metastases. Theranostics. 2018; 8: 1966-84.
65. Xue S, Wang Y, Wang M, Zhang L, Du X, Gu H, et al. Iodinated oil-loaded, fluorescent mesoporous silica-coated iron oxide nanoparticles for magnetic resonance imaging/computed tomography/fluorescence trimodal imaging. Int J Nanomedicine. 2014; 9: 2527-38.
66. Yang RSH, Chang LW, Wu J, Tsai M, Wang H, Kuo Y, et al. Persistent tissue kinetics and redistribution of nanoparticles, quantum dot 705, in mice: ICP-MS quantitative assessment. Environ Health Perspect. 2007; 115: 1339-43.
67. Longmire M, Choyke PL, Kobayashi H. Clearance properties of nano-sized particles and molecules as imaging agents: considerations and caveats. Nanomedicine (Lond). 2008; 3: 703-17.
68. Zhao L, Peng J, Huang Q, Li C, Chen M, Sun Y, et al. Near-infrared photoregulated drug release in living tumor tissue via yolk-shell upconversion nanocages. Adv Funct Mater. 2014; 24: 363-71.
69. Brown RP, Delp MD, Lindstedt SL, Rhomberg LR, Beliles RP. Physiological parameter values for physiologically based pharmacokinetic models. Toxicol Ind Health. 1997; 13: 407-84.